

**ELECTRICAL STEEL STACKS FOR TRACTION MOTORS – FUNDAMENTAL INVESTIGATIONS OF THE WELDABILITY**T. Schade<sup>1</sup>, J. Pflomm<sup>1</sup>, D. Shakirov<sup>1</sup>, J. P. Bergmann<sup>2</sup><sup>1</sup>Robert Bosch GmbH, Robert-Bosch-Str. 2, D - 71701 Schwieberdingen<sup>2</sup>Technische Universität Ilmenau, Neuhaus 1, D - 98684 Ilmenau**ABSTRACT**

For new innovative electrical machine concepts, the joining technologies have to fulfill enhanced requirements concerning reliability and reproducibility. Laser welding enables new prospects for the design of the elements guiding the magnetic flux. However, the stacked design of these machine elements represents a challenging factor regarding the development of a robust laser welding process. This paper presents a simulative approach of both the temperature field and the distortion of electrical steel due to laser welding. Furthermore welding experiments were carried out to investigate the weldability of the electrical steel stack. These results enhance the understanding of a welding process on a stacked workpiece. Moreover, a significant influence of different process variables is outlined. Thus compressive stress, which is applied on the stack design, showed a significant influence on the weldability.

**Index Terms – Electrical steel, silicon steel, laser welding, simulation, distortion**

**1. INTRODUCTION**

Key components in electrical machines are the stacks made out of electrical steel. They conduct and force the magnetic flux and reduce the eddy current losses due to their laminated design [1], [2]. The electrical steel sheets are made out of coiled material by cutting technologies. Subsequently, they are placed on top of each other and are fixed by joining technologies, e.g. interlocking, gluing or welding. The demands concerning the stack accuracy and stability are high [1]. So far the joints have to resist only static stress requirements - in general they are a mounting aid for the assembly of the machine. For new, innovative machine concepts, e.g. machines with segmented rotors or stators, the joining technologies have to fulfill additional requirements like reliability and reproducibility. The common welding technology to produce electrical steel stacks is TIG welding. However, the possible weld seam geometries are limited by use of this joining process. Additionally, this process is restricted by limited welding speed ( $f < 1$  m/min) and the minimum thickness of weldable electrical steel sheets (0.35 mm). These restrictions can be overcome by a laser welding process [1]. According to ISO/TR 581:2005 [3] the weldability depends on three influencing variables: welding process, design and material, Fig. 1.

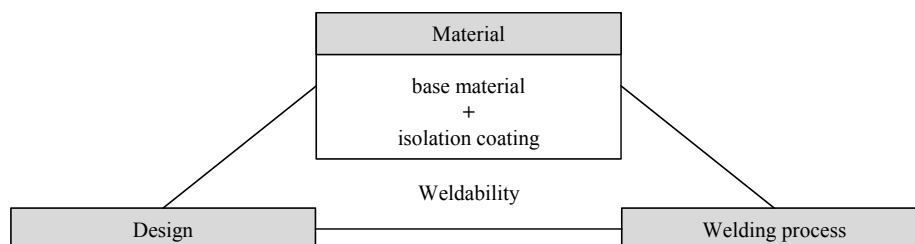


Fig. 1. Weldability, referring to ISO/TR 581:2005 [3]

During the welding process the isolation coating, which is applied on both sides of each steel lamella, is decomposed by the thermal heat input in the welding zone and adjacent areas. The decomposition products of the coating can cause seam defects e.g. pores and cracks [1], [4] additional to pores generated by the laser welding process itself [5]. Up to now, a feed rate reduction was considered as the main control variable to affect the welding result while joining electrical steel stacks with a laser welding process [1], [4]. However, this reduction results in an increase of the thermal energy input which leads to unwanted effects, e.g. an increase in welding distortion and thermal influenced area next to the weld seam. Additionally to that, the cycle time during production increases. Thus, in practice this is not a sufficient method. For the designing of durable weld seams it is essential to characterize the mechanical strength of the weld seam. This work shows investigations concerning the weldability of electrical steels and different ways to investigate and evaluate welded electrical steels.

## 2. METHOD

### 2.1 Methodology and validation of the finite element analysis

The FE-analysis was performed using the Abaqus commercial code, provided by Simulia. First, the response to the welding process was calculated for a single electrical steel sheet. Once the simulation methodology was verified using the single sheet configuration (Fig. 2, left side) the methodology was transferred to calculate the response to the welding process for a stacked configuration (Fig. 2, right side).

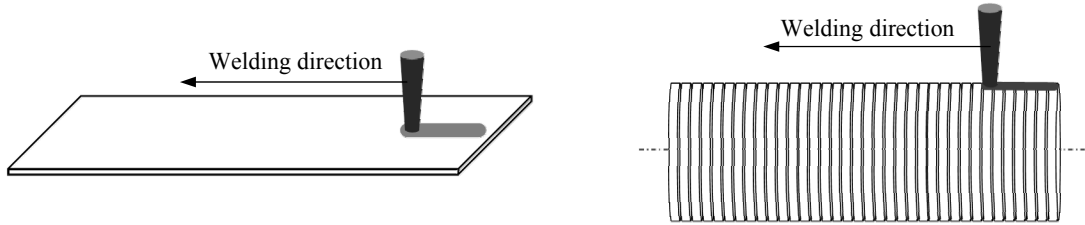


Fig. 2. Left side: schematic representation of the single sheet welding experiment; right side: schematic representation of the stacked configuration

Laser welding itself is a highly transient and complex process. In order to simulate this process in a reasonable time, simplifications are necessary. If the mechanical solution does not influence the thermal solution, it is valid to compute the thermal behavior first and use this data to calculate the mechanical behavior in addition [6]. This assumption was made since in case of the single sheet configuration, the local distortion due to the thermal load is small and the contribution to heat conduction due to fluid dynamics is neglected. As a consequence of this separation, a phenomenological surrogate heat source is used. This heat source consists of cylindrical and ellipsoid structures. Its primary purpose is to create a weld pool which closely resembles the weld pool generated by the laser welding process. Therefore, it is not necessary to model the fluid dynamics inside the weld pool. The distribution of laser power inside the heat source follows a bell curve. The resulting temperature field is adapted to known parameters such as laser power, focal diameter and isotherms due to solidification or phase transformation. Fig. 3, left side, shows such an isotherm due to solidification of the molten pool. The investigated electrical steel (M330-35A) showed no phase transformation while cooling down from solidification temperature to ambient temperature. Hence, no isotherms of phase transformation are detectable in the cross section. To ensure a proper adaption of the surrogate heat source, the actual temperature field  $T(x, y, z, t)$  was captured with thermocouples; type K, wire diameter 80  $\mu\text{m}$ , sampling frequency 300Hz. The thermocouples were spot welded on the test specimen, Fig. 3, right side.

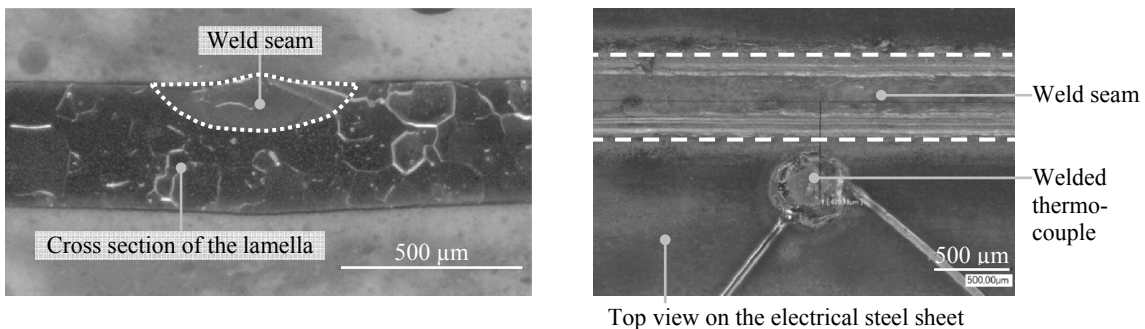


Fig. 3. Left side: cross section of a weld seam, solidification isotherm is outlined white; right side: top view on a weld seam made on the single sheet configuration and a thermocouple, located at a distance of  $\Delta z = 630 \mu\text{m}$  from the weld seam center

To validate a proper functionality of the spot welded thermocouples, the temperature output signal was compared to the ambient temperature and the temperature of boiling water (measured deviation  $< \pm 1 \text{ K}$ ). Their distance to the weld seam was measured after the welding experiment, using a digital light Microscope. The effects of the isolation coating on the welding process of the single sheet configuration were neglected. However, all relevant material properties were assumed to be temperature dependent. The thermal conductivity, specific heat, elastic modulus and Poisson's ratio were calculated using the software JMatPro 6.0. The thermal expansion also was calculated using JMatPro 6.0 but additionally was verified with dilatometer experiments. The temperature dependent yield curves were obtained using a "Gleeble" system.

The displacement of the single sheet configuration, shown in Fig. 4, was captured contactless with a laser triangulation measuring system.

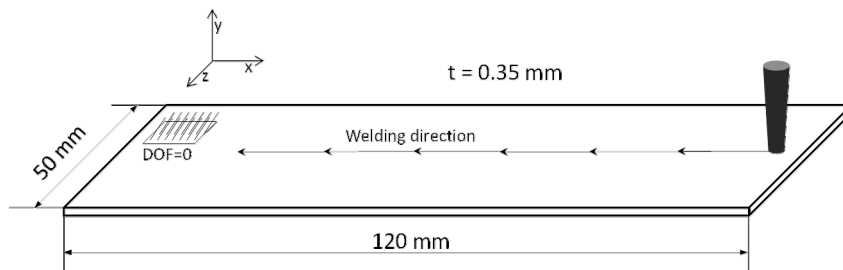


Fig. 4. Schematic representation of the single sheet welding experiment, using a statically determined mechanical constraint; one area of support with fully locked degrees of Freedom (DOF)

In contrast to the single sheet configuration, the effects of the isolation coating on the stacked configuration, Fig. 5, cannot be neglected. The isolation coating greatly influences the models local and global thermal conductivity. Additionally, its isolating properties are removed at those points where the sheets were welded together. Therefore it is necessary to capture this behavior. Taken this into account, additional dependencies were fitted into the material model. Hence, those parts of the isolation coating, which reached the liquidus temperature of the basis material, received the material properties of the basis material for the remaining time of the simulation. The stacked configuration was modeled as a single bulk, i.e. the nodes between the individual lamellas were merged. The isolating properties were modeled by modifying the thermal conductivity of the nodes, lying directly between the lamellas. Heat exchange between the lamellas due to convection and radiation was neglected. In order to avoid a violation of the continuity equation and the law of energy conservation, the values of density and specific heat of the isolation coating were assumed to be equal to the values of the basis material.

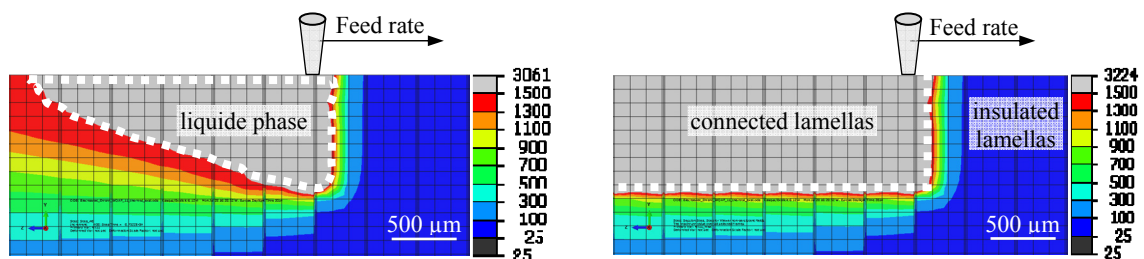


Fig. 5. FE-Analysis of the temperature field for a stacked design; left side: capture of a single step, displaying the molten bath; right side: visualization of the nodes which reached melting temperature, displaying the actual weld seam

## 2.2 Methodology of the weldability experiment

Detached from the specimen for the validation of the simulation model, the welding experiments were carried out on a welding specimen, Fig. 6, left side. This electrical steel disc is coated with an EC-5 isolation varnish on both sides. For the welding experiments, several of these specimens were stacked and the generated stack was preloaded with compressive stress. The weld seam was produced at the circumference in axial direction, Fig. 6, right side, using a 1 kW continuous wave disc laser with a wave length of 1030 nm.

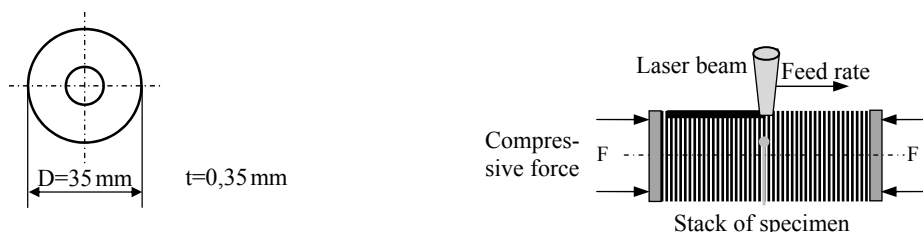


Fig. 6. Experimental investigation of the welding process, left side: design of the specimen; right side: experimental set up

Characteristic for welding of electrical steel stacks is a sensitivity to pore formation due to thermal decomposition of the isolation coating between the electrical steel lamellas [1]. These gaseous decompositions products exhaust under high pressure during the welding process from the welding zone. The gaseous decomposition products are not only crossing the molten pool but are also forced through the gaps between the

lamellas [1]. In Order to investigate the weldability, a basis configuration of several process factors was chosen. The generated weld seams, using this basis configuration, shown in TABLE I, are afflicted with a constant amount of pores. Based on this configuration, individual factors were varied and the results examined. To verify the process reproducibility, the variation of the process had been examined in advance. The pore ratio showed a scatter band of 5.56% which was spread evenly around the average value (n=5 specimens of the basis configuration).

TABLE I Experimental setup for the basis configuration

Factor	Factor Adjustment
Material	M250-35A
Thickness of the isolation coating	1.2 $\mu\text{m}$
Focal diameter	300 $\mu\text{m}$
Feed rate	2 m/min
Compressive stress	0.2 N/mm <sup>2</sup>
Penetration depth	900 $\mu\text{m}$
Exhaust flow	70 dm <sup>3</sup> /s

In order to quantify the pore content, the weld seams were grinded in the longitudinal weld seam direction. The pores containing area and the total weld seam area were measured with a digital light microscope, an example is shown in Fig. 7. The pore ratio was defined as: the summation of the area of pores divided by the total weld seam area. This ratio was used to evaluate the quality of the weld seams.

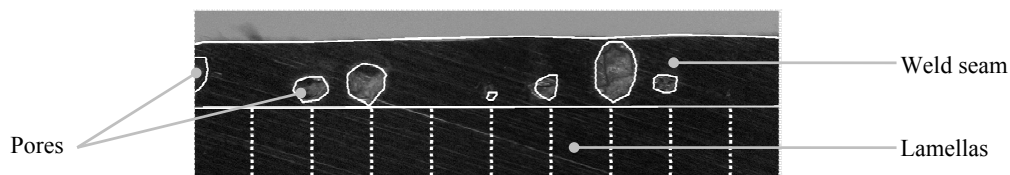


Fig. 7. Longitudinal section of a weld seam, evaluation of the pore ratio according to the pore containing area and the total weld seam area

### 3. RESULTS

#### 3.1 FE-Analysis of the welding process

##### 3.1.1 Temperature Field

The calculated temperature field of the single sheet configuration confirms the assumption of high temperature gradients and shows a good match with the measured temperature field, Fig. 8, left side.

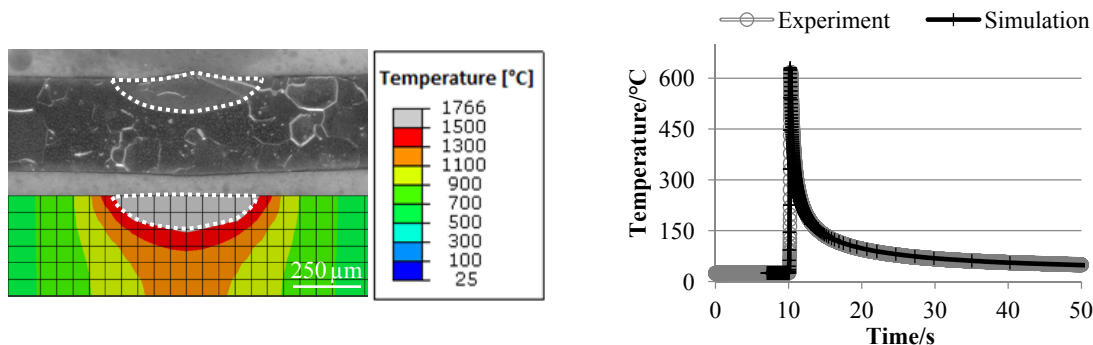


Fig. 8. Left side: comparison between the welding experiment and simulation, molten pool outlined white; right side: temperature vs. time at a distance of approximately 630  $\mu\text{m}$  from the weld seam center; Single sheet configuration, heat conduction welding, base material M330-35A, nominal laser power  $P_L = 200 \text{ W}$ , focal diameter  $d_f = 300 \mu\text{m}$ , feed rate  $f = 1 \text{ m/min}$

Furthermore, the calculated and measured temperature-time curves for equivalent points at the single sheet specimen and the FE-mesh show an obvious agreement. Fig. 8, right side, shows the match for a point at 630  $\mu\text{m}$  distance from the weld seam center.

The maximum temperatures reached during the process (Fig. 9, left side) are also an indicator for the accuracy of the simulation. The simulation slightly underestimates the maximum temperature. The largest difference is approximately 18K at 1900 $\mu\text{m}$  distance from the weld seam center. In case of coated electrical steels, the maximum temperatures reached during the welding process are important, since the majority of isolation coatings are temperature sensitive. The decomposition of these coatings influences the efficiency of the electrical machines they are built-in and further more significantly effects the weldability of electrical steel stacks.

### 3.1.2 Displacement (nomenclature according Fig. 4)

According to the calculated temperature field  $T(x, y, z, t)$  the mechanical response of the model was analyzed. Fig. 9, right side, shows the comparison between simulation and experiment of the displacement  $u_y(x)$  for the single sheet configuration. Close to the mechanical constraint the simulation delivers a good estimation of the displacement. However, with growing distance to the constraint the offset grows to an amount of roughly 3 mm. Thereby three major mechanisms were identified causing the gap between simulation and experiment.

**Internal stress:** While running the first welding experiments with the single sheet configuration, the direction in which the sheet bent due to the distortion of the laser welding process was random. This unexpected behavior could be assigned to the residual internal stresses, which remained in the sheet despite the annealing process, which is typical for “full finished” electrical steel grades. After an additional annealing process (4h, 650°C) the sheets always bent in the same, estimated direction. However, annealing processes do not eliminate internal stresses completely. A little amount of residual internal stresses always remains. Their orientation and magnitude and therefore their influence on the welding result is unknown.

**Geometric Imperfections:** Geometries, produced by manufacturing processes always show a variation of quality [7]. In case of a thin sheet, an arbitrary geometric imperfection, except a global reduction in the thickness, will result in an increase in the section modulus. However, the simulation assumes a perfectly equal distribution of the thickness throughout the whole model. This leads to an underestimation of the actual bending stiffness and therefore to an overestimation of the actual distortion  $u_y(x)$ .

**Superposition of Errors:** The results delivered by the simulation will generally show a certain amount of deviation to the reality. In case of the investigated experimental setup (Fig. 4), the displacement at the end of the sheet  $u_y(x = 120)$  is strongly influenced by minor errors occurring next to the constraint. Their magnitude in displacement will be superimposed with increasing distance to the constraint.

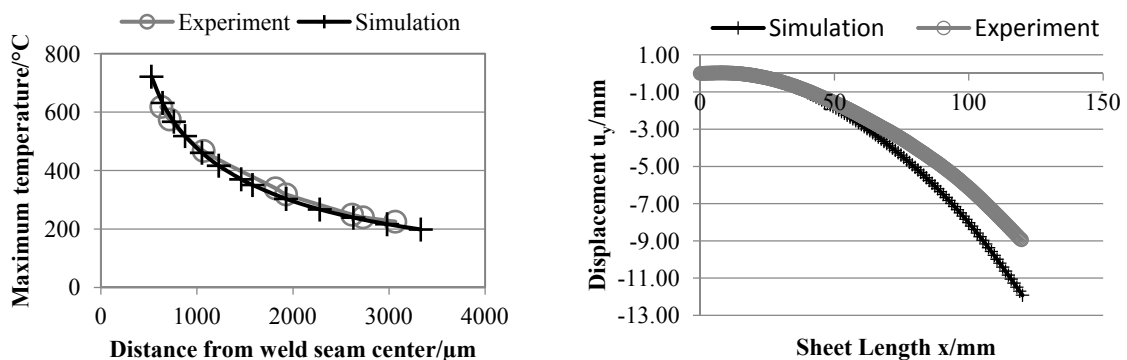


Fig. 9. Left side: maximum temperature reached vs. the distance from the weld seam center; right side: displacement  $u_y(x)$  vs. the sheet length; single sheet configuration, heat conduction welding, base material: M330-35A, nominal laser power  $P_L = 200\text{ W}$ , focal diameter  $d_f = 300\ \mu\text{m}$ , feed rate  $f = 1\text{ m/min}$

## 3.2 Experimental investigation of the welding process

### 3.2.1 Influence of the compressive stress

In a test series, using the basis configuration (Fig. 6, right side), the influence of an axial preload on the electrical steel stack was examined.

In a concept model two possibilities for the escape of the gaseous decomposition products during the welding process were expected which interfere with each other.

- The gaseous decomposition products rise through the molten pool and escape through the surface of the molten pool
- The gaseous decomposition products escape through the gaps between the lamellas.

The total resistance against the degassing pressure on these two ways is a parallel circuit of the degassing resistances. Due to manufacturing tolerances, the lamellas don't fit closely together, but contact each other in a few contact points. With increasing compressive stress on the stack, the amount of contact points increases, too. This growth is exponentially and depends on the scatter of the surface roughness. Simultaneously, the mean

distance of the lamella is decreasing. By variation of the mean lamella distance the degassing resistance through the gaps between the lamella is varied.

A compression test was performed to evaluate the relative shortening of a lamination stack under compressive stress. The resulting graph, Fig. 10, left side, shows a retarded increase of the compressive stress for a little relative shortening Fig. 10, left side (1), but a linear growth for a high relative shortening, Fig. 10, left side (2). The characteristic curve change initiates at compressive stress of about  $4.2 \text{ N/mm}^2$ . This indicates a reduction of the mean distance between the electrical steel lamellas which is superposed by the deformation of the lamination stack. A linear elastic behavior assumed, the total compliance of the stack design is the combination of the compliance of the lamella base material and the isolation coating. The determined total compression modulus for the linear section in diagram Fig. 10, left side, is  $18,000 \text{ N/mm}^2$ . Nevertheless, the high amount of the actual compression stress suggests the assumption, that a linear elastic behavior is hardly probable, at least for the isolation coating.

As mentioned in 2.2, the weld seams made with the parameters of the basis configuration are afflicted with a constant pore ratio. The evaluation of the pore ratio against the compressive stress shows a strong increase of the pore ratio for rising compressive stress, Fig. 10, right side (3). The gradient fades into saturation for higher compressive stress Fig. 10, right side (4). The highest tested compressive stress was  $15.2 \text{ N/mm}^2$ . Furthermore, the results are indicating a connection between the mean lamella distance and the pore formation process which strengthens the introduced concept model. For increasing compressive stress the mean lamella distance is decreasing and thus the degassing resistance trough the gaps between the lamellas rises. For high compressive stress the mean lamella distance is changing only very slowly. At the same time the pore ratio is not rising anymore because a constant resistance for the degassing through the lamella gaps is achieved and a big part of the gaseous decomposition products are escaping through the molten pool.

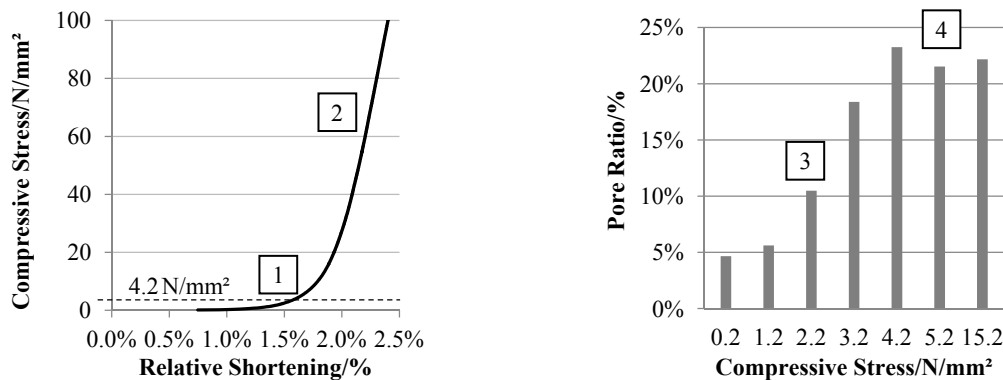
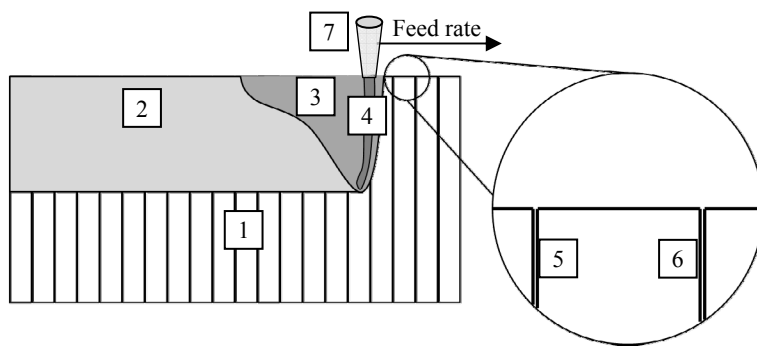


Fig. 10. Left side: compressive stress vs. relative shortening of the stack configuration; right side: pore ratio of the weld seam vs. compressive stress on the stack configuration, deep penetration welding, base material: M250-35A, nominal laser power  $P_L = 470 \text{ W}$ , focal diameter  $d_f = 300 \mu\text{m}$ , feed rate  $f = 2 \text{ m/min}$

### 3.2.2 Model of the feed rate influencing the weld seam properties

During laser welding of electrical steel stacks the feed rate has a significant influence on the pore formation [1]. This is shown in a test series in which the feed rate was varied, using the basis configuration mentioned in 2.2.

In the following part a model to describe the influence of the feed rate on the pore formation is introduced. Because of a dependence of the geometrical, material and the process factors on the pore formation, the following classification by concrete feed rate figures is only valid for the examined factor configuration. However, by adjustment of the class limits, a transfer of the presented model on other factor configurations is possible. Clarification about the nomenclature concerning the laser welding process of lamination stacks provides Fig. 11. The model distinguishes three feed rate ranges for a deep penetration laser welding process. An overview about the model is given by TABLE II



1	Stack configuration
2	Solid weld seam
3	Molten pool
4	Keyhole
5	Leading edge of lamella
6	Rear edge of lamella
7	Laser beam

Fig. 11. Nomenclature of the stack welding process

#### Low Feed Rate ( $f \leq 1 \text{ m/min}$ )

Welding with low feed rates, a lot of heat hurries ahead the molten pool due to thermal conductivity. During this process, the thermal front in feed rate direction tilts forward: on top of the weld seam the distance between the thermal front and molten pool is bigger than the distance at the bottom of the weld seam. This causes a molten connection on top of the lamellas before the deepest point of the molten pool reaches the gap between the lamellas. Through this metallic connection a part of the heat is already transferred to the next lamella, resulting in a constant welding depth from the leading to the rear edge of the lamellas. During the welding process, a high energy input per unit length is induced to the stack due to the low feed rate. The result is the formation of a high volume of molten bath and at the same time a high amount of gaseous decomposition products of the isolation coating. However, the high volume of molten material and the high energy input per unit length results in a long period of time until the solidification of the weld seam is complete. Hence, the gaseous decomposition products have enough time to escape through the molten pool to the weld seam surface. Therefore no pores were detectable after welding with low feed rates.

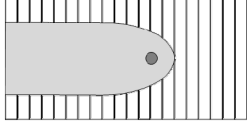
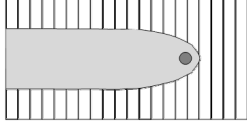
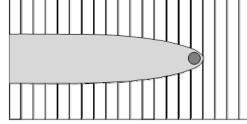
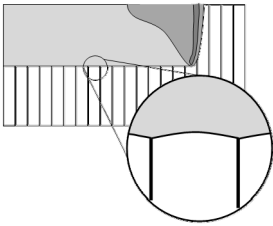
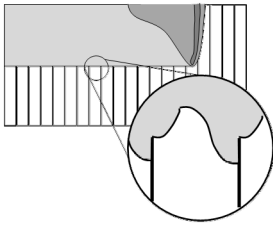
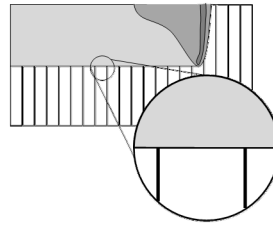
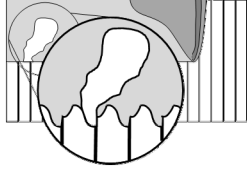
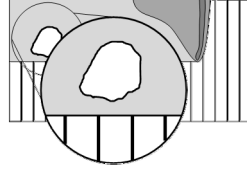
#### Medium Feed Rate ( $1 \text{ m/min} < f < 3 \text{ m/min}$ )

Welding with medium feed rates, less heat hurries ahead the molten pool. This causes less tilt of the thermal front. Hence, a molten connection between two lamellas develops later in comparison with low feed rates. When the thermal front reaches the gap between adjacent lamellas, the deepest point of the molten pool is already near the rear edge of lamella one. Because there isn't a molten connection between the adjacent lamella yet, the heat is conducted to the inside of the stack. Thus the depth of the molten pool increases on the rear edge of the lamella. At the same time, the heat which is causing the deepening of the molten pool is not transferred to the following adjacent lamella anymore. If the molten pool reaches this lamella, there is a big temperature drop which leads to a significant decrease in welding depth at the leading edge from the next lamella. Global, a tooth-shaped profile of the welding depth is forming. During this process, the gaseous decomposition products of the isolation coating are also forming in the deepened area of the molten pool at the rear edge of the lamellas. The long distance to the weld pool surface and the reduced period of time until the molten pool solidifies, prevents the escape of the gaseous products. These products are overtaken by the solidification front and therefore they remain as pores in the weld seam.

#### High Feed Rate ( $f > 3 \text{ m/min}$ )

With high feed rates only little heat hurries ahead the molten pool. Therefore the front and the deepest point of the molten pool nearly match each other. Hence, at the transition between adjacent lamellas heat accumulation does not take place because no heat is hurrying ahead anymore. Thus, the welding depth is constant over the complete lamella width.

TABLE II Model of the feed rate influencing the weld seam properties

Property	Property Value		
	f < 1 m/min	1 m/min < f < 3 m/min	f > 3 m/min
Feed rate	f < 1 m/min	1 m/min < f < 3 m/min	f > 3 m/min
Amount of heat hurrying ahead	↑	→	↓
Position of the deepest point and the front of the molten pool			
Period of time where a point at the weld seam surface is in its liquid phase (calculated via FE-Analysis)	0.194 s @ 0.5 m/min, 300 W	0.059 s @ 2 m/min, 440 W	0.019 s @ 8 m/min, 900 W
Welding depth from leading to rear edge of the lamella			
Characteristic shape of the pores	No pores in this feed rate band		

### 3.2.3 Evaluation of the Pore Ratio

The evaluation of the grindings in longitudinal weld seam direction confirms the model of the feed rate influence on the pore formation, Fig. 12, left side. The pore content of the weld seams, which is quantified by the pore ratio, is near zero percent for feed rates  $f \leq 1$  m/min, Fig. 12, left side (1). This indicates a complete degassing of the gaseous decomposition products. For feed rates of  $f = 2$  m/min and  $f = 4$  m/min the pore ratio is increasing significantly, Fig. 12, left side (2). This is ascribed to an increased trapping of gaseous decomposition products in the weld seam. Assumed that the amount of isolation coating in the molten pool is limited, the amount of gaseous decomposition products which can be caught by the solidification front is also constricted. Hence the gradient of the pore ratio versus the feed rate is decreasing with higher feed rates. This is shown by Fig. 12, left side (3).

### 3.2.4 Characteristic shape of the pores

Furthermore, clues about the shape of the pores and the profile of the welding depth for the different feed rates are possible. For the feed rates of  $f \leq 1$  m/min the grindings are not showing any significant pores, Fig. 12, right side (4). For a feed rate of  $f = 2$  m/min the variation of the penetration depth between the lamella leading edge and the lamella rear edge becomes visible for several lamellas. Fig. 12, right side (5), is showing a deepening of the molten pool on the rear edge of the lamellas as an origin of pore formation. Thus, the pore shape develops backward in the area of the higher welding depth. With increasing height it tilts in welding direction and lower viscosity. The welding depth at the leading edge of the following lamella is distinctly lower. These results are in match with the introduced model.

For feed rates of  $f = 4$  m/min and  $f = 8$  m/min the pore formation at the gap between the lamellas is not recognizable anymore. With increasing feed rate the characteristic pore shapes become rounder, Fig. 12, right side (6), an indication for the separation from the feeding accumulation zone under the weld seam.



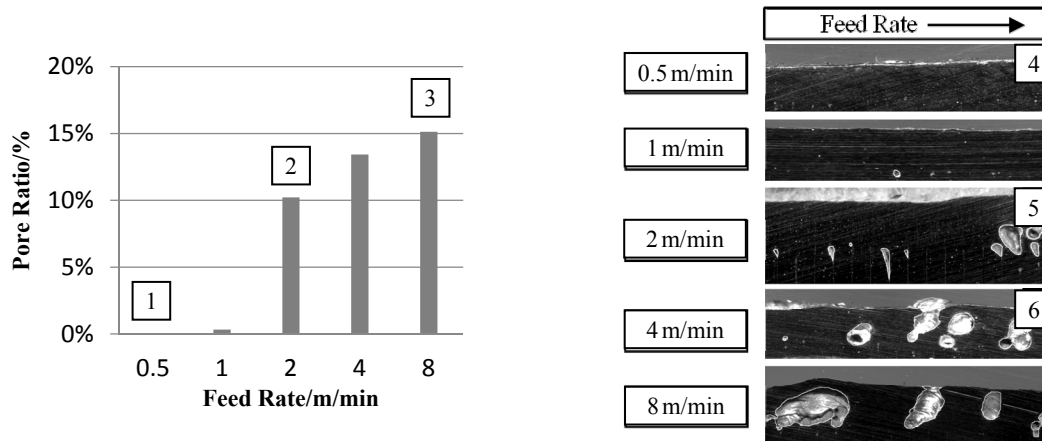


Fig. 12. Left side: pore ratio of the weld seam vs. feed rate of the laser process; right side: characteristic shape of the pores according to the feed rate; base material: M250-35A, focal diameter  $d_f = 300 \mu\text{m}$ , const. welding depth  $s_{wd} = 900 \mu\text{m}$

#### 4. CONCLUSION

The dynamic thermal and mechanic response of electrical steel was calculated using FE-analysis techniques. The computed prediction of the temperature field matches the measurement. The mechanical response to the welding process is predicted with a little overestimation of the distortion. The existence of internal stresses in M330-35A was detected, despite the executed annealing process which was performed after rolling the electrical steel sheet. Modeling techniques for the welding process of a stacked electrical steel configuration are established using finite element methods.

The influences of the compressive stress and the feed rate on the pore formation in the weld seam during the welding of lamination stacks were examined. Two models for the description of the influences were developed. They were validated by experiments, afterwards. A significant increase of the pore content for rising compressive stress is demonstrated. Furthermore, an increase of the feed rate causes a rise of the pore content, too. In addition, the influence of different feed rate regimes for welding lamination stacks is shown.

#### 5. ILLUSTRATIONS, GRAPHS, AND PHOTOGRAPHS

- Fig. 1. Weldability, referring to ISO/TR 581:2005 [2]
- Fig. 2. Left side: schematic representation of the single sheet welding experiment; right side: schematic representation of the stacked configuration
- Fig. 3. Left side: cross section of a weld seam, solidification isotherm is outlined white; right side: top view on a weld seam made on the single sheet configuration and a thermocouple, located at a distance of  $630 \mu\text{m}$  from the weld seam center
- Fig. 4. Schematic representation of the single sheet welding experiment, using a statically determined mechanical constrain; one area of support with fully locked degrees of Freedom (DOF)
- Fig. 5. FE-Analysis of the temperature field for a stacked design; left side: capture of a single step; right side: visualization of the memorized maximum temperatures, displaying the penetration depth of the weld seam
- Fig. 6. Experimental investigation of the welding process, left side: design of the specimen; right side: experimental set up
- Fig. 7. Longitudinal section of a weld seam, evaluation of the pore ratio according to the pore containing area and the total weld seam area
- Fig. 8. Left side: comparison between the welding experiment and simulation, molten pool outlined white; right side: temperature vs. time at a distance of approximately  $630 \mu\text{m}$  from the weld seam center; Single sheet configuration, heat conduction welding, base material M330-35A, nominal laser power  $P_L = 200 \text{ W}$ , focal diameter  $d_f = 300 \mu\text{m}$ , feed rate  $f = 1 \text{ m/min}$
- Fig. 9. Left side: maximum temperature reached vs. the distance from the weld seam center; right side: displacement  $u_y(x)$  vs. the sheet length; single sheet configuration, heat conduction welding, base

material: M330-35A, nominal laser power  $P_L = 200 \text{ W}$ , focal diameter  $d_f = 300 \mu\text{m}$ , feed rate  $f = 1 \text{ m/min}$

Fig. 10. Left side: compressive stress vs. relative shortening of the stack configuration; right side: pore ratio of the weld seam vs. compressive stress on the stack configuration, deep penetration welding, base material: M250-35A, nominal laser power  $P_L = 470 \text{ W}$ , focal diameter  $d_f = 300 \mu\text{m}$ , feed rate  $f = 2 \text{ m/min}$

Fig. 11. Nomenclature of the stack welding process

Fig. 12. Left side: pore ratio of the weld seam vs. feed rate of the laser process; right side: characteristic shape of the pores according to the feed rate; base material: M250-35A, focal diameter  $d_f = 300 \mu\text{m}$ , const. welding depth  $s_{WD} = 900 \mu\text{m}$

## REFERENCES

- [1] N. Brachthäuser, A. De Paoli, P. Schäfer, G. Senn, Laserstrahlschweißen von paketierte Elektroblechen, ATZproduktion, number 03, p. 38–43, 2011
- [2] C. D. Wuppermann, A. Schoppa, Merkblatt 401- Elektroband und -blech, Stahl-Information-Zentrum, Düsseldorf, 2005
- [3] ISO/TR 581:2005, Weldability, Metallic materials – General principles, p. 5, 2007
- [4] K. Dickmann, Lasereinsatz bei Elektroblechen – Technologische Untersuchungen zur Schweißbarkeit von Elektroblechen mit Hochleistungslasern, technica, die Fachzeitschrift für die Maschinen-, Elektro und Metallindustrie, number 40/05, p. 27-33, 1991
- [5] A. Matsunawa, Observation of Keyhole and Molten Pool Behaviour in High Power Laser Welding, Mechanism of Porosity Formation and Its Suppression Method, Transactions of JWRI 30(1) P.13-P.27, 07/2001
- [6] D. Radaj, Wärmewirkung des Schweißens – Temperaturfeld, Eigenspannungen, Verzug, Springer-Verlag, 1988
- [7] DIN EN 10106, Kaltgewalztes nicht kornorientiertes Elektroblech und – band im schlussgeglühten Zustand, deutsche Fassung EN 10106:2007, 2007

## CONTACTS

M. Sc. Till Schade

till.schade@de.bosch.com

Univ.-Prof. Dr.-Ing. habil. Jean Pierre Bergmann

jean.pierre.bergmann@tu-ilmenau.de